

Article

Phytochemical Exploration of Ceruchinol in Moss: A Multidisciplinary Study on Biotechnological Cultivation of *Physcomitrium patens* (Hedw.) Mitt.

Carlos Munoz^{1,*}, Kirsten Schröder¹, Bernhard Henes¹, Jane Hubert², Sébastien Leblond³, Stéphane Poigny¹, Ralf Reski⁴ and Franziska Wandrey¹

¹ Mibelle Group Biochemistry, Mibelle AG, 5033 Buchs, Switzerland; stephane.poigny@mibellegroup.com (S.P.)

² NatExplore SAS, 51140 Prouilly, France

³ PatriNat (OFB, MNHN), 12 Rue Buffon, CP39, 75005 Paris, France

⁴ Plant Biotechnology, Faculty of Biology, University of Freiburg, Schaezlestraße 1, 79104 Freiburg, Germany

* Correspondence: carlos.munoz-hernando@mibellegroup.com

Abstract: The moss *Physcomitrium patens* (*P. patens*), formerly known as *Physcomitrella patens*, has ascended to prominence as a pivotal model organism in plant biology. Its simplicity in structure and life cycle, coupled with genetic amenability, has rendered it indispensable in unraveling the complexities of land plant evolution and responses to environmental stimuli. As an evolutionary bridge between algae and vascular plants, *P. patens* offers a unique perspective on early terrestrial adaptation. This research involved the biotechnological cultivation of *P. patens*, followed by a deep phytochemical investigation of two extracts covering a large polarity range together using an NMR-based dereplication approach combined with GC/MS analyses. Subsequently, a multidisciplinary approach combining bioinformatics, in-silico techniques, and traditional methods was adopted to uncover intriguing molecules such as the diterpene ceruchinol and its potential receptor interactions for future cosmetic applications. The kaurene diterpene ceruchinol, representing up to 50% of the supercritical CO₂ extract and also identified in the hydroalcoholic extract, was selected for the molecular docking study, which highlighted several biological targets as CAR, AKR1D1, and 17β-HSD1 for potential cosmetic use. These findings offer valuable insights for novel uses of this plant biomass in the future.

Keywords: *Physcomitrium patens*; bryophyte; ceruchinol; biotechnology; molecular profiling; molecular docking



Citation: Munoz, C.; Schröder, K.; Henes, B.; Hubert, J.; Leblond, S.; Poigny, S.; Reski, R.; Wandrey, F. Phytochemical Exploration of Ceruchinol in Moss: A Multidisciplinary Study on Biotechnological Cultivation of *Physcomitrium patens* (Hedw.) Mitt. *Appl. Sci.* **2024**, *14*, 1274. <https://doi.org/10.3390/app14031274>

Academic Editor: Anna Waszkielewicz

Received: 21 December 2023

Revised: 27 January 2024

Accepted: 30 January 2024

Published: 3 February 2024



Copyright: © 2024 by the authors. Licensee MDPI, Basel, Switzerland. This article is an open access article distributed under the terms and conditions of the Creative Commons Attribution (CC BY) license (<https://creativecommons.org/licenses/by/4.0/>).

1. Introduction

A prominent model organism for plant biology research is *Physcomitrium* (*Physcomitrella*) *patens*, also known as the spreading earth moss. It provides a unique opportunity to study plant evolution and development [1–4]. With a genome size of about 480 megabases, *P. patens* has been thoroughly sequenced and annotated, providing the basis for extensive genomic research [5]. Its haploid-dominant life cycle is noteworthy for enabling genetic manipulation, making it a valuable asset for scientific exploration [6].

The moss's accessibility in experimental settings is a significant advantage. It boasts a short generation time, easy axenic cultivation in the laboratory, and genetic transformation capabilities [7]. Moreover, its high regenerative capacity provides ample opportunities to study developmental processes and responses to environmental stimuli [8,9]. Positioned exquisitely in the evolutionary spectrum of plant life, *P. patens* is an excellent model to investigate the origins and adaptations of terrestrial plants. Studies of *P. patens* have elucidated the transition from aquatic to terrestrial ecosystems, the evolution of plant structures, and the acquisition of traits needed to thrive on land [10,11].

The moss's unique developmental characteristics, particularly its dominant haploid phase, the gametophyte, comprising protonema and gametophore, provide an excellent context for investigating the complexities of plant reproduction and growth. Investigations into the regulatory mechanisms of cell differentiation, gametogenesis, and sporogenesis in this moss have provided insights that have broader relevance to plant development as well as its physiology and structure [12–15], its relationship against aggressors and with the outside [16,17]. In sum, *P. patens* has assumed a pivotal role as a model organism in the fields of evolutionary and developmental biology, bridging gaps in our comprehension of early terrestrial plant life.

The *P. patens* adult gametophyte, the gametophore, has a cuticle whose chemical composition and structural features are similar to those of flowering plants. This suggests that this played a pivotal role in the transition of plants to terrestrial environments, effectively regulating water status and providing protection against biotic and abiotic stressors. Moreover, research involving mutant plants with reduced cuticular wax accumulation supports the notion that the gene responsible for cuticle wax formation in *P. patens* is evolutionarily conserved across different plant species, including *Arabidopsis thaliana* (L.) Heynh., suggesting its early emergence during the terrestrial invasion of plants [4,18–21].

Despite *P. patens* cuticle having a relatively thinner profile compared to vascular plants, it plays a pivotal role in reducing water loss and providing defense against desiccation and environmental stressors. The intricate structure comprises two primary components: cutin, a polyester matrix of hydroxy fatty acids, diacids, and glycerol, and a variety of waxes. The wax elements consist of very-long-chain fatty acids (VLCFAs), primary and secondary fatty alcohols, fatty ketones, aldehydes, alkanes, wax esters, and nonaliphatic elements such as triterpenoids and flavonoids [22].

Cutin, composed of hydroxy and epoxy fatty acids, creates a waterproof barrier that significantly reduces water loss [23]. The presence of cutin, along with suberin, another essential lipid polymer rich in fatty acids within the cuticle, facilitates water conservation and adaptation to diverse environmental conditions. This intricate interplay of lipids within the cuticle underscores its vital role as a crucial interface, facilitating the moss's ecological success in various habitats. As the cutin and waxy layer are presented as a protective threshold with external aggressors and contamination, the elucidation of its composition is paramount [18,22–27].

Although *P. patens* is well known from a genetic point of view, references about its constituents are scarce. In the literature, there are references to Kaurane derivatives in cuticles and gametophytes of various mosses besides *P. patens* [28–30]. In this study, the phytochemical profile of *P. patens* grown using biotechnological tools was deeply investigated. Two different extracts were produced to get a general picture of *P. patens* constituents on a wide polarity range: a non-polar supercritical CO₂ extract was prepared from the plant biomass material left after multiple washes, and an aqueous extract. These two extracts give a global molecular identification of the major metabolites by combining hydrophilic and lipophilic extraction and analytical conditions.

As one significant marker of both extracts, we focused on ceruchinol ((-)-(16S)-Kauran-16-ol, Figure 1), which, like other tetracyclic diterpenes, shows a remarkable prevalence in lichen species and various vascular plants [29,31–35]. Our objective was to evaluate the potential of ceruchinol for a commercial application and to generate a proposal for similar research in the future.

The beneficial functions of *P. patens* extracts containing ceruchinol in topical applications were also investigated in this work. For this purpose, we used in-silico approaches to identify potential interactions of ceruchinol with human receptors expressed in skin cells. This, together with the other information on *P. patens* components in this study, can help in the development of commercial applications for moss extracts.

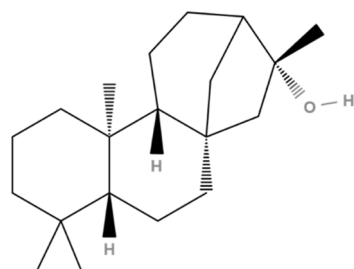


Figure 1. Ceruchinol ((-)-(16S)-Kauran-16-ol).

2. Materials and Methods

2.1. Plant Material and Generation of *P. patens* Biomass

P. patens was grown as an axenic protonema culture with a modified Knop medium [36–38] in a 20 L wave Bioreactor (Wave System 20/50 EHT, Sartorius, Göttingen, Germany) under continuous white light for a period of 3 weeks. Room temperature was set at 20 °C, and the culture aerated with an airflow of 10 L/h enriched with 2% CO₂. The obtained biomass, composed of protonemata and gametophores (Figure 2) images obtained with a Digital Microscope VHX-7000 from KEYENCE, Mechelen Belgium), was filtered over a 60 µm nylon mesh, and the culture medium was disposed of. The filtered biomass was then dispersed in water with a T25 Ultraturrax (IKA, Staufen, Germany) at 20,000 rpm. Subsequently, the material was pressed at 150 bars in a HAFICO-press (Fischer Maschinenfabrik, Mönchengladbach, Germany) in order to extract the water-soluble compounds (Figure 3). The resulting biomass cake was utilized for CO₂ extraction for the isolation of non-polar components.

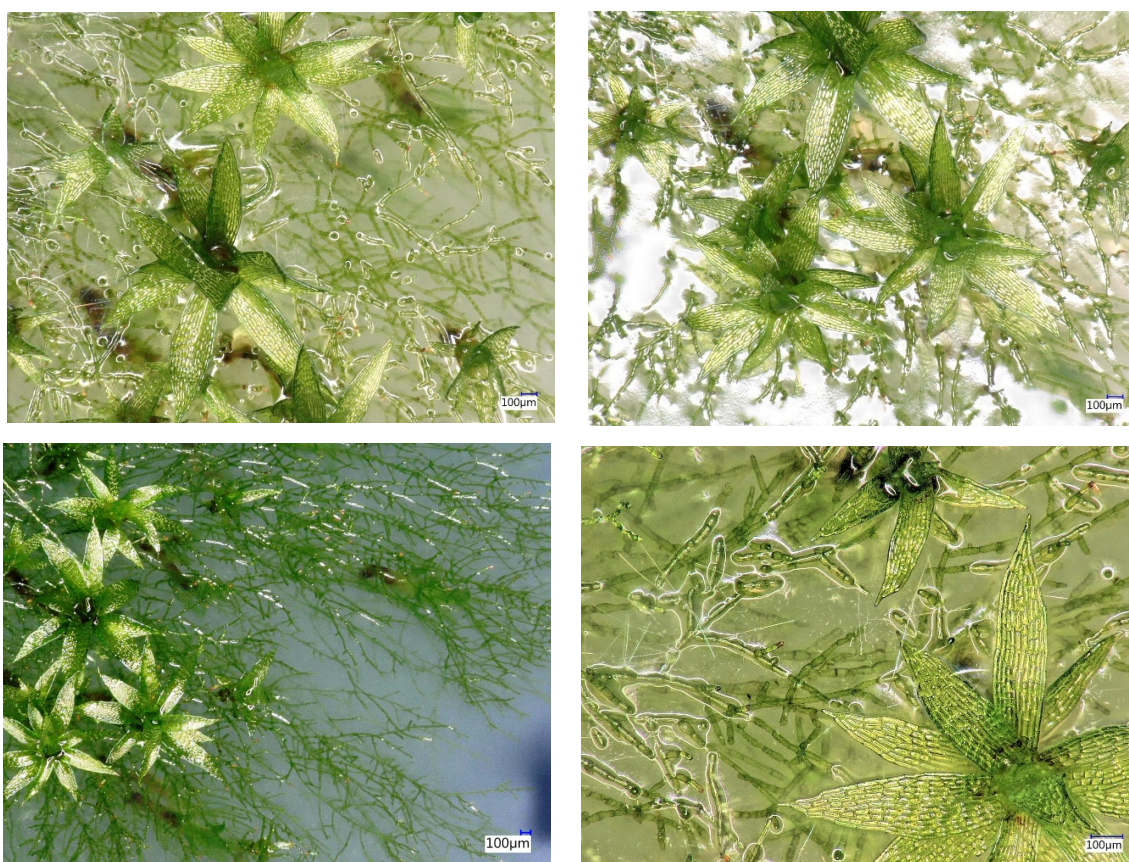


Figure 2. Microscope photographs from the cultivated *P. patens* before harvesting showing the presence of protonemata and gametophores.

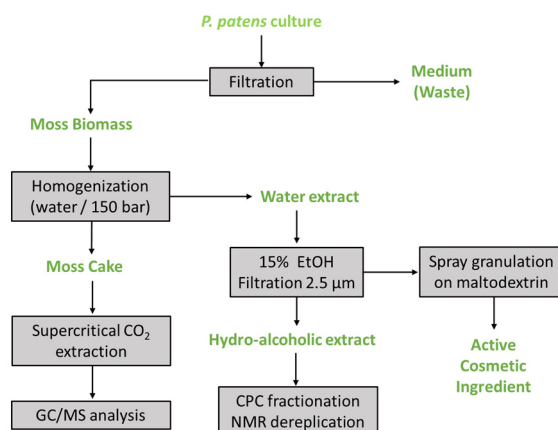


Figure 3. Workflow of the production of the water-based cosmetic ingredient as well as the CO₂ *P. patens* extract used for the composition analysis.

The water-soluble components were combined with ethanol to reach a final concentration of 15% for the purpose of preservation. Subsequently, this mixture was filtered through a 2.5 µm Begerow (Eaton, Germany) filter to remove the insoluble cell debris. The resulting hydroalcoholic extract was fractionated by Centrifugal Partition Chromatography (CPC), and the fractions were analyzed by NMR for metabolite identification, with a primary focus on examining the water-soluble components.

2.2. Centrifugal Partition Chromatography (CPC)

The hydroalcoholic extract was fractionated by CPC using a column containing 7 partition disks engraved with a total of 231 twin cells of 1 mL (FCPC200[®], Rousselet Robatel Kromaton, Annonay, France) connected to a Blueshadow pump 80P (Knauer, Berlin, Germany) and a Labocol Vario 4000 collector (Knauer). The biphasic solvent system was ethyl acetate/acetonitrile/*n*-butanol/water (6/6/1/7, *v/v*). The lower phase was used as the stationary phase at 12 mL/min. The column rotation speed was set at 1500 rpm. 3189 mg of the hydroalcoholic extract were dissolved in 11 mL of stationary phase plus 5 mL of mobile phase and loaded into the CPC column by a 20 mL loop. The upper phase of the solvent system (mobile phase) was pumped in the ascending mode for 100 min. At the end of the experiment the most polar compounds retained in the column were recovered in the descending mode for 15 min. Fractions were collected every minute and combined according to their high-performance thin-layer chromatography (HPTLC) profiles. HPTLC was performed on a CAMAG[®] system (ATS4 autosampler, ADC2 developing chamber, and a visualizer 2). Fractions were spotted on pre-coated silica gel 60F254 HPTLC Merck plates and developed with the mixture acetate/water/acetic acid/formic acid (10/2/1/1, *v/v*). Visualization was performed under UV light at 254 and 366 nm and under visible light after spraying the dried plates with 50% H₂SO₄ and vanillin, followed by heating. A total of 10 final fractions were obtained.

2.3. NMR Analyses and Metabolite Identification

Fractions F01-F10 were dissolved in 600 µL of DMSO-*d*₆ and analyzed by ¹³C NMR at 298 K (Bruker Avance AVIII-600 TCI cryoprobe, Karlsruhe, Germany). The uniform driven equilibrium Fourier transform (UDEFT) sequence was used with 512 scans, an acquisition time of 0.36 s, and a relaxation delay of 3 s. All spectra were phased and baseline-corrected using TOPSPIN 4.0.5 (Bruker). The absolute intensities of all ¹³C NMR signals were automatically collected in the spectra of the ten fractions and exported to a table using an in-house bucketing script (size of the buckets 0.3 ppm). The table was imported into PermutMatrix 1.9.3 (LIRMM, Montpellier, France) for hierarchical clustering analysis (HCA). As a result, ¹³C NMR chemical shift clusters were visualized as dendrograms on a 2D map (Figure 4). The higher the intensity of ¹³C NMR signals, the brighter the color on

the map. For metabolite identification, each ^{13}C NMR chemical shift cluster observed in the heatmap was submitted to an in-house NMR database comprising the structures and predicted chemical shifts of natural molecules ($n \approx 9000$ in November 2023) (interface from ACD/NMR Workbook Suite 2012, ACD/Labs, Ontario, Canada). Additional homonuclear correlation spectroscopy (COSY), heteronuclear single-quantum coherence (HSQC), and heteronuclear multiple bond correlation (HMBC) spectra were also acquired to confirm, correct, or re-orientate database proposals to the right chemical structures.

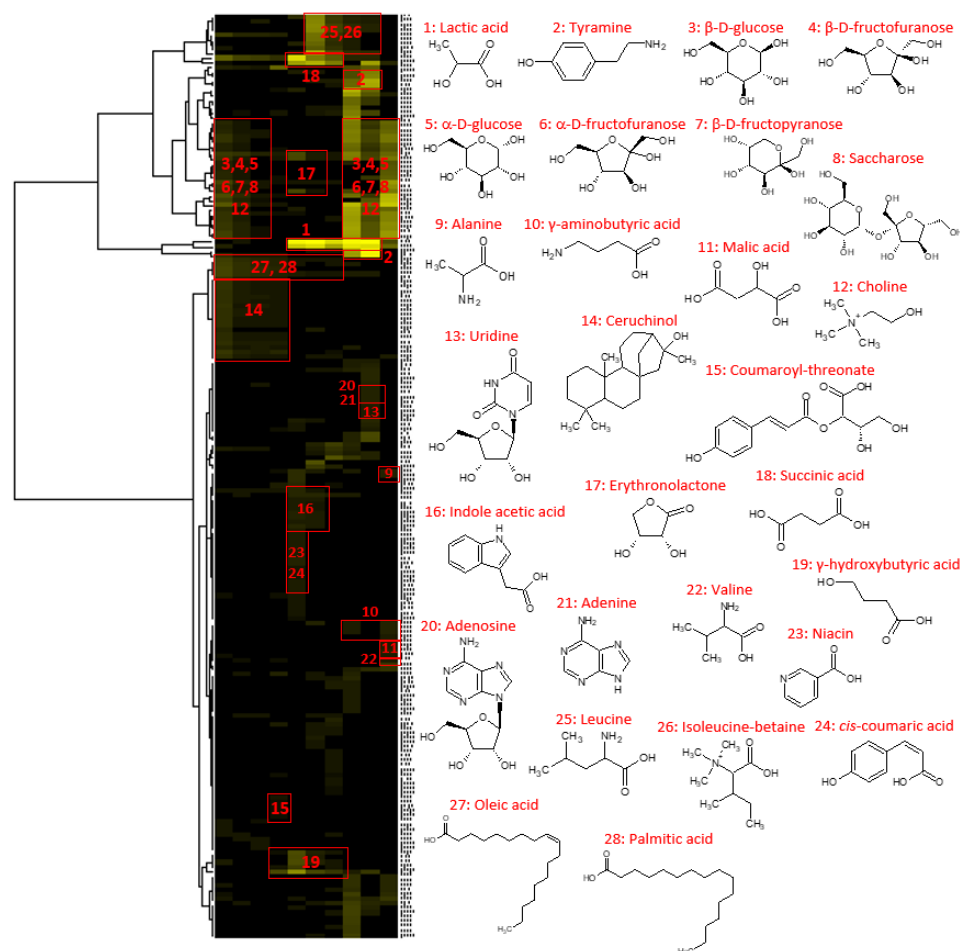


Figure 4. HCA correlation map of ^{13}C NMR signals with the identified compounds.

2.4. Supercritical CO_2 Extraction

Approximately 5 g of dried biomass (Moss cake, see Figure 2) was accurately weighed and introduced into the extraction cell and placed in an autoclave maintained at 40°C . The first extraction was performed with 100% CO_2 at a flow rate of 30 g/min and 300 bars of pressure. Unfortunately, it was unable to extract anything under these conditions.

A second extraction was performed with the addition of ethanol. The CO_2 flow was 30 g/min, and the ethanol rate was 3 g/min. A mass of 5.0022 g was accurately weighed, then introduced into an extraction cell placed in an autoclave maintained at 40°C and 300 bars for one hour. The extraction yield was calculated at 54.65% obtaining therefore 2.7342 g of material.

2.5. GC-MS Analyses

GC/MS analyses of the CO_2 extract were performed on a 7890A GC coupled with a 5977A MSD single quadrupole manufactured by Agilent (Santa Clara, CA, USA). 1 μL of a solution of the extract in ethanol at 1 mg/mL was injected in split mode with the ratio 102:1. The injector temperature was set to 250°C . The DB-5ms capillary column was used with

the following dimensions (30 m × 0.25 mm × 0.25 µm film thickness). Helium was used as the carrier gas at a flow rate of 1 mL/min. The column temperature was programmed from 40 °C (5 min) to 300 °C at 3 °C/min. The final temperatures were held for 10 min. The total GC cycle time was 101.67 min. The transfer line temperature was set to 250 °C. The ion source and the quadrupole were maintained at 230 °C and 150 °C, respectively. Electron ionization (EI) mass spectra were recorded at 70 eV in positive mode, in the range m/z 30–1000, using full SCAN mode (Total Ion Chromatogram). All data were recorded using ChemStation v 10.0. The mass spectrum peaks considered as confirmed for analysis were those that matched at least 80% of the library. Peaks were identified by comparison with mass spectrometer libraries (HPCH 2205, ISIPCA, and NIST14). Three software programs were used with different algorithms for identification confirmation (ChemStation v 10.0, Unknowns Analysis, and Mass Hunter).

Results were obtained using MSD Chem software (Agilent technologies, Santa Clara, CA, USA) and supplemented with those obtained using analysis deconvolution software to check for co-elution (two or more compounds under a single peak).

2.6. Ligand-Based and Docking Screening

Preparation of compounds:

The aim of the in-silico analyses performed by the company Pharmacelera was to identify a list of potential protein targets for each compound using computational methods. The compounds were virtually prepared using the Ligand Preparation module of PharmScreen[®] software (Version 5.2.0) [39]. PharmScreen[®] (PS) field-based virtual screening software uses a unique and superior 3D representation of molecules based on electrostatic, steric, and hydrophobic interaction fields derived from semi-empirical Quantum-Mechanics (QM) calculations. Such fields describe with high accuracy the factors that determine ligand/receptor interactions.

PS Ligand Preparation step included:

- Calculation of 3D conformers and selection of more representative ones in terms of energy and root mean squared deviation (RMSD).
- Calculation of molecular charges (Gasteiger method) and LogP (atom-type method).

The resulting compounds were used as reference compounds for the Virtual Screening module of the PS software.

2.7. Preparation of Co-Crystallized Compounds Extracted from Protein Data Bank (PDB) Database (DB)

The PDB database was used to identify potential targets for the list of reference compounds (Figure 5). This database contains crystallographic information on protein-compound complexes. The information can be used to extract the bioactive conformation (the conformation adopted in the protein binding site) of a compound and compare its similarity with the reference compounds.

In order to obtain the final list of compounds from the PDB in their bioactive conformation, the PDB database was curated by selecting targets with at least one co-crystallized compound. From the selected targets, elements such as peptides, compounds used to stabilize the crystallization process were discarded. Compounds from repeated chains of the PDB structure of the complex were also removed.

Once compounds from PDB were identified, they were also prepared using PS Ligand Preparation module, calculating the charge and LogP values as indicated in the previous step.

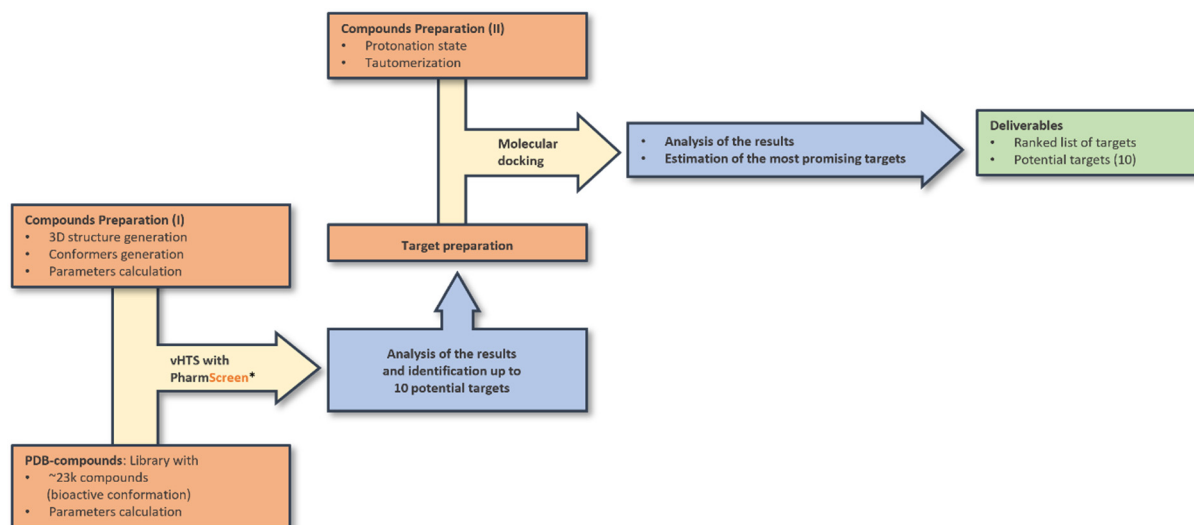


Figure 5. Workflow for the ligand preparation, ligand-based virtual screening, and molecular docking. * Selection of ligands based on chemical structure and available biological information on potential targets.

2.8. Ligand-Based Virtual Screening with PS

The PS Virtual Screening module was used to align and calculate the similarity of each reference compound to each PDB compound. PS uses the calculated 3D molecular fields to align and measure similarity based on these 3D physicochemical descriptors. As a result of this virtual screening campaign, a list of potential targets was generated based on the similarity of the reference compounds to the co-crystallized compounds of each target extracted from the PDB. A list of up to 10 targets per compound was considered to apply a docking protocol. In the case of ceruchinol, after an evaluation of the different targets obtained for this molecule, a list of 3 different potential targets passed to the docking step.

2.9. Docking of Ceruchinol against Selected Targets

To validate the prediction made during the ligand-based virtual screening campaign using PS, ceruchinol was docked against the selected targets using DockThor [40]. The following steps were applied:

- The selected target was prepared for the docking protocol (missing side-chains, duplicated amino acids, pH).
- For some of the targets, different PDB structures were found in the PDB database. Structures with the best resolution were selected. In the case of flexible regions, the most representative structure was chosen.
- Protonation state and tautomerization were calculated.
- Co-crystallized compounds were docked against their own target to validate the docking protocol, evaluating its capacity to retrieve the same pose available in the PDB.
- If multiple cavities were found, compounds were docked in each of them.

To evaluate and select the best docking poses, four different terms were used:

- The interaction energy (E_I), which is given by the sum of the van der Waals and electrostatic interaction energies.
- The total energy (E_{tot}), which is calculated by combining (i) the intermolecular interaction energy calculated as the sum of the van der Waals and electrostatic potentials between the protein–ligand atom pairs, (ii) the intramolecular interaction energy calculated as the sum of the van der Waals and electrostatic potentials between the 1–4 atom pairs, and (iii) the torsional term of the ligand.
- The affinity prediction or docking score (S), which is evaluated using an empirical function that considers the Total Energy of the top-ranked pose.

- The root-mean-square deviation (RMSD), which is calculated by comparing the atomic coordinates of each binding mode with those of a reference ligand and measures the average distance between the atoms of the two molecules.

Additionally, and to support the previous information, a visual evaluation of each pose was done to assess the interactions (hydrogen bonds, polar, hydrophobic, etc.) between the compound and the residues in the binding pocket as well as the similarity of the pose to the co-crystallized compound.

3. Results

3.1. Chemical Profiling of the Hydroalcoholic Extract

The hydroalcoholic extract was fractionated by CPC in a total of 10 fractions eluted in increasing order of polarity. All fractions were analyzed by 1D and 2D NMR, but ^{13}C NMR data were first used to build the dereplication workflow. Bucketing of ^{13}C peaks across the ten fractions resulted in a table of 10 columns (ten CPC fractions) and 202 rows corresponding to the NMR buckets (Δ 0.3 ppm) for which a ^{13}C peak was detected in at least one CPC fraction. This table was submitted to HCA. In this way, ^{13}C NMR signals belonging to the same molecule were aggregated as in a heatmap presented in Figure 4. For each cluster, database proposals were confirmed or re-oriented to the right chemical structures by rigorously scrutinizing ^1H - ^{13}C and ^1H - ^1H correlations in HSQC, HMBC, and COSY spectra. As a result, 28 *P. patens* metabolites were unambiguously identified using this NMR-based identification process.

As illustrated in Figure 4, the most polar fraction F10, which represented \approx 94% of the crude extract mass, was mainly composed of simple sugars (glucose, fructose, and saccharose), as well as amino acids, choline, γ -aminobutyric acid, and malic acid. The less polar fractions F01–F04, representing \approx 1.5% of the extracted mass together, were characterized by the presence of the diterpene ceruchinol, as well as fatty acids in the mixture. Lactic acid and succinic acid were significant compounds detected in fractions F05–F09, recovered during the elution step and representing \approx 5% of the extracted mass. Other minor compounds of fractions F05–F09 exhibited a high chemical diversity; they included, for instance, coumaroyl-threonate, indole acetic acid, erythronolactone, niacin, leucine or leucine-betaine, tyramine, uridine, and adenosine.

The identification of gibberellin members, family of phytohormones that control various developmental events, including elongation of stems, germination, dormancy, budding, flower development, and senescence of leaves and fruits [41], including Kaurane derivatives like ceruchinol may suggest a potential role in the maturation processes of *P. patens*. These compounds could act as precursors, laying the groundwork for the formation of the wax layer. Some fatty acids like C16 and C18 were also identified in our analysis.

Another noteworthy discovery was the existence of indole-3-acetic acid (IAA), a type of auxin. The presence of this auxin is of particular significance, as it is recognized for its role in facilitating caulonema formation and maturation in mosses [24]. This multifaceted molecule may suggest a nuanced interplay of hormonal and structural factors that may collectively contribute to the intricate processes involved in the development of wax layers in *P. patens*.

3.2. GC-MS Profiling of the Supercritical CO_2 Extract

Supercritical fluid extraction was performed on the moss cake with the aim of identifying non-polar components that may have been excluded from the aqueous extraction in the previous section. In addition to components previously identified in the earlier extract, such as C16 or C18, which were found in higher concentrations in this extraction, the predominant compound discovered was ceruchinol. Other Kaurane derivatives like Kaur-15-ene and Kaur-16-ene were also detected in the CO_2 extract.

Furthermore, potential substrates or products of suberin polymerization [42] were detected in the extract, including derivatives of cinnamic acid, long-chain aldehydes, and secondary alcohols. This finding provides additional support for our assumption regarding

the composition of the protonemata and gametophores of *P. patens*, reinforcing the notion that the moss may exhibit a complex makeup involving these identified compounds. The GC-MS analysis of the supercritical CO₂ extract resulted in the signals shown in Figure 6 and Supplementary Figure S1.

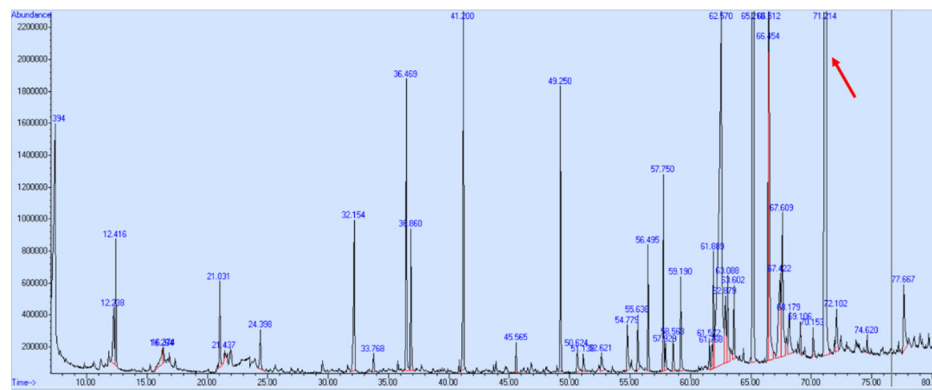


Figure 6. GC-MS profile of the supercritical CO₂ extract at 1 mg/mL in EtOH. Total ion current obtained. Ceruchinol was detected at Tr = 71.21 min (red arrow) and corresponds to the major peak. At Supplementary Figure S1 one could see the same graphic but without any zoom in order to reveal the importance of the ceruchinol peak.

Comparison of the sample with internal standards showed that ceruchinol was present as a major peak and eluted at a retention time of 71.21 min.

Other molecules were as well profiled, as shown in Table 1, particularly long-alkyl chain lipidic constituents and terpenoids, among which significant kaurene diterpenes.

Table 1. Molecules detected at the Supercritical CO₂ extract. Ceruchinol appears as Kauran-16-ol at 71.21 min. PK: Peak, RT: Retention time, CAS numbers, Area: surface under peak.

PK	RT	Library/ID	CAS	Qual	Area	Confirmed?
1	7.39	Acetic acid	64-19-7	86	1.30 × 10 ⁸	Yes
2	12.24	HEXANAL	66-25-1	93	30,055,867	Yes
3	21.03	2-Octen-1-ol, (Z)-	26001-58-1	93	25,079,272	Yes
4	24.4	9.14 Benzene acetaldehyde	122-78-1	87	14,788,190	Yes
5	32.15	15.77 Dodecane	112-40-3	95	56,976,919	Yes
6	33.77	2-Cyclopenten-1-one, 2-methyl-	1120-73-6	89	5,702,674	Yes
7	36.47	19.71 Thymol	89-83-8	95	72,963,027	Yes
8	36.86	20.14 Carvacrol	499-75-2	95	37,180,865	Yes
9	41.2	24.61 Tetradecane (C14)	629-59-4	97	1.14 × 10 ⁸	Yes
10	45.57	Butylated Hydroxytoluene	128-37-0	97	7,402,971	Yes
11	49.25	32.89 Hexadecane (C16)	544-76-3	98	63,206,613	Yes
12	50.62	Benzene, 1-methyl-4-[(1-methylethylidene)cyclopropyl]-	24578-28-7	71	9,609,670	Yes
13	51.14	34.73 Amyl cinnamaldehyde<Z->	101365-33-7	99	6,484,050	Yes
14	52.62	1-Methyl-5-nitro-1H-benzimidazol-2-ol	66108-85-8	65	9,853,674	Yes
15	54.78	39.42 Cinnamaldehyde<2-hexyl-(Z)->	364364-06-7	99	17,036,726	Yes
16	55.64	38.90 Benzyl benzoate	120-51-4	95	17,676,783	Yes
17	56.49	40.40 Octadecane (C18)	593-45-3	98	28,462,303	Yes

Table 1. Cont.

PK	RT	Library/ID	CAS	Qual	Area	Confirmed?
18	57.75	3,7,11,15-Tetramethyl-2-hexadecen-1-ol	102608-53-7	87	40,608,898	Yes
19	57.93	Hexa-hydro-farnesol	6750-34-1	93	8,759,193	Yes
20	58.56	9-Eicosyne	71899-38-2	81	11,027,985	Yes
21	59.19	BENZYL SALICYLATE (ALLERGENE)	118-58-1	87	28,689,063	Yes
22	61.57	44.98 Beyerene	2359-73-1	99	9,040,448	Yes
23	61.77	Biformen	5957-33-5	83	6,353,250	Yes
24	61.89	45.59 Pimaradiene	1686-61-9	99	34,535,194	Yes
25	62.57	n-Hexadecanoic acid	57-10-3	99	4.01×10^8	Yes
26	62.88	47.09 Ethyl hexadecanoate	628-97-7	94	32,838,290	Yes
27	63.09	47.33 Eicosane (C20)	112-95-8	98	30,418,475	Yes
28	63.6	47.25 Kaur-15-ene	5947-50-2	99	21,893,926	Yes
29	65.22	48.66 Kaur-16-ene	562-28-7	99	7.40×10^8	Yes
30	66.45	50.22 Benzyl cinnamate	103-41-3	95	74,793,795	Yes
31	68.18	Octadecanoic acid	57-11-4	98	24,803,583	Yes
32	69.11	53.54 Docosane	629-97-0	93	7,580,271	Yes
33	70.15	Kaur-15-ene, (5 α ,9 α ,10 β)-	511-85-3	87	7,534,955	Yes
34	71.21	Kauran-16-ol (Ceruchinol)	5524-17-4	90	1.44×10^9	Yes
35	72.1	Arachidonic acid	506-32-1	95	19,255,524	Yes
36	74.62	7-Methyl-Z-tetradecen-1-ol acetate	959269-58-0	92	4,176,098	Yes
37	77.67	Dipalmitin	761-35-3	91	34,085,962	Yes
38	91.75	Glycerol tricaprylate	538-23-8	81	4.31×10^8	Yes
39	92.75	Cholesta-8,24-dien-3-ol, 4-methyl-,	7199-92-0	95	41,964,203	Yes
40	94.37	Campesterol	474-62-4	87	2.36×10^8	Yes
41	95.04	Cholesta-6,22,24-triene, 4,4-dimethyl-	1000128-66-9	95	4.29×10^8	Yes
42	96.01	Caprin	621-71-6	70	1.46×10^8	Yes

Like ceruchinol, Kaurane diterpenes represent a class of organic compounds characterized by a distinctive tetracyclic diterpene skeleton. Structurally, they consist of four fused rings, with variations in functional groups and side-chain modifications contributing to their diverse bioactivities. These compounds are prevalent across various plant taxa, such as Annonaceae, Asteraceae, and Lamiaceae, exhibiting significant pharmacological properties, including anti-inflammatory, anticancer, and antimicrobial activities. They are particularly important in bryophytes such as liverworts, where ongoing research has led to the discovery of novel derivatives that are being pursued for their bioactive potential [43,44].

Kaurane diterpenes, with their unique structural features, exhibit diverse bioactivities and play significant roles in the ecological narratives of both mosses and fungi. In mosses, they contribute to defense mechanisms and adaptive responses, while in fungi, they act as defenders and potential influencers of ecological relationships.

These compounds are thought to fortify the resilience of mosses against herbivores or pathogens. Additionally, their potential involvement in adaptive responses to environmental conditions, such as light, temperature, and moisture fluctuations, adds complexity to their putative functions. The alleged properties of Kaurane diterpenes suggest a role in safeguarding mosses against microbial threats, contributing to the overall ecological fitness of these bryophytes.

In fungi, Kaurane diterpenes were conceived as chemical defenses against competing microorganisms; these compounds contribute to the ecological niche protection of fungi. Beyond defense, the participation of Kaurane diterpenes in mutualistic associations with plants introduces the intriguing prospect of influencing host-fungus relationships and broader ecological dynamics. Within the intricate landscape of fungal secondary metabolism, Kaurane diterpenes take on the role of potential signaling molecules, influencing diverse cellular processes and facilitating communication within fungal communities.

3.3. Docking Evaluation

With the goal of expanding the potential applications of these extracts, we decided to undertake a coupling and docking approach involving one of the most intriguing molecules identified. Given that some derivatives of Kaurane were present, and one of them, ceruchinol, emerged as the most abundant component in the supercritical fluid extract, we directed our focus towards a coupling study with various targets using bioinformatics tools.

This decision reflects our commitment to explore the diverse applications of the identified compounds, particularly those rich in ceruchinol. By employing bioinformatic tools, we sought to elucidate potential interactions and applications of this compound with various targets, thereby broadening the scope of our study beyond the initial identification and characterization of molecular components in *P. patens*. This coupling approach serves to enhance the translational relevance of our findings, opening avenues for future applications and developments based on the rich molecular repertoire extracted from the moss.

As described in the methods section, a pool of 23,000 total candidates was scouted, leading to a selected list of 10 possible candidates, where the three most interesting ones were selected and further analyzed. This selection was based on market analysis and other criteria, such as the relevance of these receptors in skin biology and the possibility of using the obtained results for later efficacy testing of potential active ingredients.

- CAR protein (Androstan Receptors)
- AKR1D1 (Aldo-keto reductase)
- 17 β -HSD1 (17 β -Hydroxysteroid dehydrogenase)

3.4. CAR Protein (Androstane Receptor)

Only a single PDB structure is currently available in the PDB database for the constitutive androstane receptor (CAR). This is the 1XNX entry describing the structure obtained from *Mus musculus* by X-ray diffraction with a resolution of 2.9 Å (Figure 7). The sequence identity with the human protein is very high (74%), and the sequence similarity is close to 85%. This suggests that 1XNX can be used with reasonable confidence to explore the potential binding of ceruchinol to this target protein.

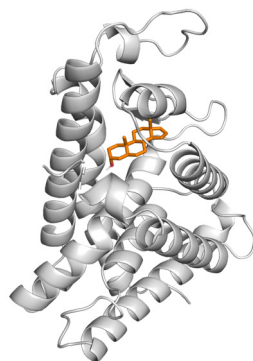


Figure 7. Structure of the constitutive androstane receptor with its unique ligand 16,17-androstene-3-ol (shown in orange).

The 1XNX structure comes with a unique ligand called 16,17-androstene-3-ol (ID: ATE), which is similar to ceruchinol (Figure 8). Before running the docking of ceruchinol, we

tested the method using ATE as a control in a redocking calculation. The result calculation indicates that the simulated pose of ATE does not coincide exactly with that of the X-ray structure, but the predicted pose is still acceptable since the positional root-mean-square deviation (RMSD) of the re-docked ligand (RMSD = 0.90 Å) is lower than 2 Å, as noted in Figure 9. The slight displacement observed between predicted and X-ray poses is most likely due to the absence of a water molecule bridging the hydroxyl group to the His²¹³ imidazole ring (note that water molecules were eliminated before the docking calculation and hence the docked ligand tends to form a direct interaction with His²¹³). The total energy (E_{tot}) is 2.3 kcal/mol, the interaction energy (E_{I}) is −31.5 kcal/mol, and the docking score (S) is −8.8 kcal/mol.

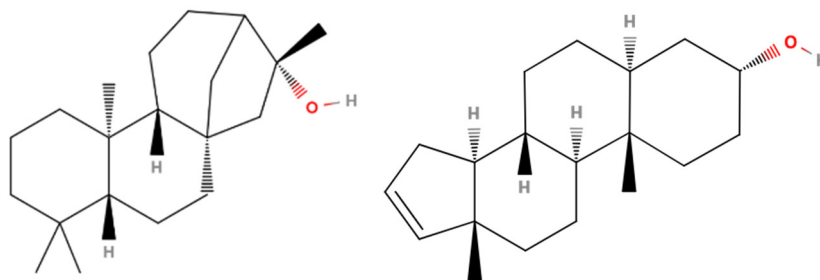


Figure 8. Chemical structure of (left) ceruchinol and (right) 16,17-androstene-3-ol (ID: ATE).

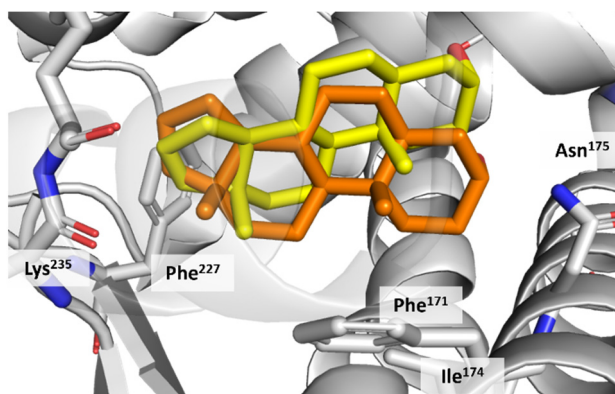


Figure 9. Result of the control docking simulation. The co-crystallized ligand is shown in orange and the re-docked ligand is shown in yellow.

Docking of ceruchinol produced two different poses with slightly different total and interaction energies but very similar docking scores (Table 2). As shown in Figure 9, the ligand is surrounded by non-polar amino acids (e.g., Phe¹⁷¹, Phe²²⁷, and Ile¹⁷⁴) which stabilise the ligand via hydrophobic interactions. In pose 1, the hydroxyl group is coordinated to Lys²³⁵ and is further stabilised via H-bond interaction. In pose 2, the nearest polar residue (Asn¹⁷⁵) is 5.0 Å away from the −OH group, but this interaction could be stabilized through a water-mediated interaction, which could be facilitated if one assumes some degree of structural plasticity in the side chains that shape the binding pocket. Considering this, the two poses are retained, and they suggest that the ligand could bind the target protein.

Table 2. Total energy, interaction energy and docking score for the two poses of ceruchinol docked to the constitutive androstane receptor.

	Total Energy (kcal/mol)	Interaction Energy (kcal/mol)	Docking Score (kcal/mol)
Pose 1	12.4	−30.1	−10.2
Pose 2	15.7	−27.0	−10.1

3.5. Docking on Human Constitutive Androstane Receptor

A model of the human CAR target was built up using sequence homology modelling and SWISSMODEL. To this end, the X-ray structure 1XNX (from *M. musculus*) was used as a template, considering the high sequence identity of 74% (as determined with BLASTP), which increases up to 85% if one considers sequence similarity (i.e., changes between residues with similar physicochemical properties). The alignment of the sequences is shown in Supplementary Materials (Additional Figure S2).

The binding site is highly conserved between the two protein models. There are few conserved changes in the residues of the pocket, mainly located in one of the edges of the binding cavity $\text{Ala}^{239} \rightarrow \text{Gly}$; $\text{Met}^{236} \rightarrow \text{Ile}$; $\text{Leu}^{253} \rightarrow \text{Phe}$; $\text{Ile}^{252} \rightarrow \text{Leu}$; $\text{Leu}^{212} \rightarrow \text{Cys}$ (Figure 10). Accordingly, it is reasonable to expect that the binding mode of the X-ray ligand will be preserved. Indeed, docking of the X-ray ligand in 1XNX in the human protein reflects the same arrangement of the crystallographic pose in the mouse protein.

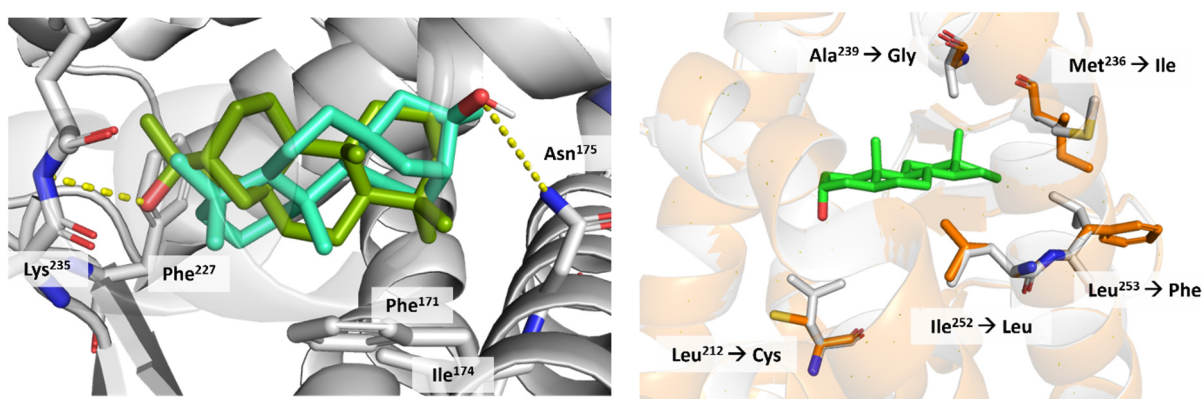


Figure 10. (Left) Result of the docking simulation of ceruchinol. Pose 1 is shown in green, and pose 2 is shown in cyan. (Right) Superposition of the human (orange) and *M. musculus* (white) CAR proteins. The position of the X-ray ligand in 1XNX is shown as green sticks, and the few changes in residues that shape the binding pocket are highlighted as sticks.

Finally, we docked ceruchinol into the human CAR model (Figure 11), and the two first poses were highly similar to the two poses retrieved from the docking in *M. musculus*, thus giving confidence to the potential binding of ceruchinol to this human target.

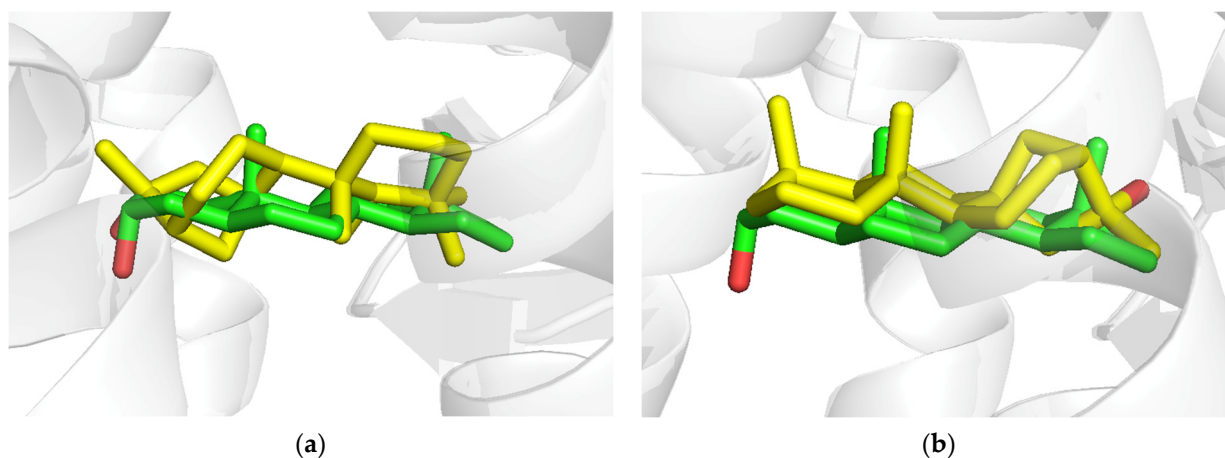


Figure 11. Results of the first two poses (a,b) were obtained from docking simulations of ceruchinol in the human CAR model. Ceruchinol is shown as yellow sticks, and the X-ray ligand (green sticks) in the pose found in 1XNX is also shown as a reference.

3.6. AKR1D1 (Aldo-Keto Reductase)

We found 14 X-ray diffraction entries with a resolution of 1.0–2.5 Å for the human 3-oxo-5-beta-steroid 4-dehydrogenase (AKR1D1) in the PDB database. All the structures feature a steroid-like ligand. Most of them also show a co-crystallized NADP molecule (Figure 12). In order to execute the docking, the PDB entry 3CAV was chosen as a representative structure due to the structural resemblance of the X-ray ligand ((5β)-pregnane-3,20-dione, ID: CI2) to ceruchinol (Figure 13).

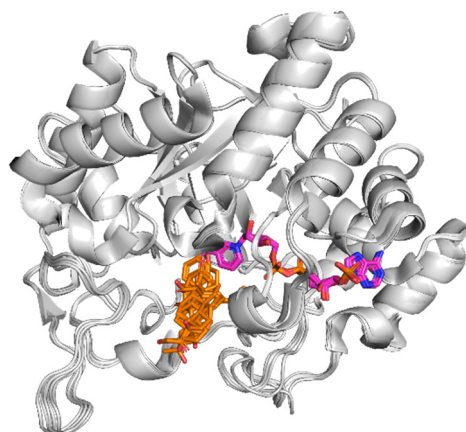


Figure 12. Superposition of selected 3-oxo-5-beta-steroid 4-dehydrogenase structural models. Co-crystallized ligands are shown in orange and cofactors NADP are shown in magenta. Showing the ensemble in the same binding site together with the NADP and presenting the alignment of the different structures.

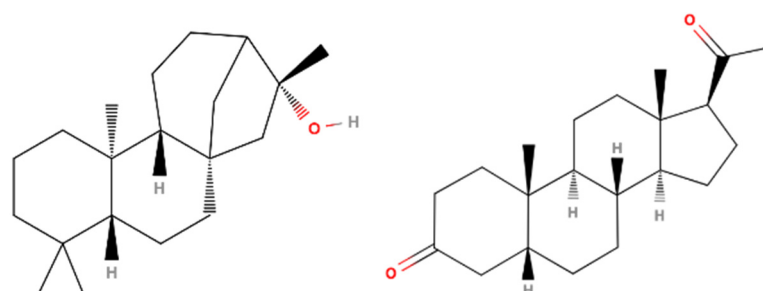


Figure 13. Chemical structure of (Left) ceruchinol and (Right) a (5β)-pregnane-3,20-dione (ID: CI2).

The redocking simulation (Figure 14 and Table 3) reproduced well the crystallographic structure (RMSD of 0.015 Å). The values of E_{tot} , E_I and S for this binding mode are 86.8, −25.2, and −9.3 kcal/mol, respectively.

Table 3. Total energy, interaction energy, and docking score for the simulated poses of ceruchinol.

	Total Energy (kcal/mol)	Interaction Energy (kcal/mol)	Docking Score (kcal/mol)
Pose 1	29.8	−25.6	−9.3
Pose 2	30.6	−25.0	−9.2

Docking of ceruchinol led to two binding modes, shown in Figure 14. They both reflect non-polar interactions with hydrophobic residues in the binding site. Pose 1 also shows the possibility of forming additional polar interactions between the hydroxyl group of ceruchinol and the carboxylate group of Glu¹²⁰ or the hydroxyl group of Tyr⁵⁸ while being close to the amide moiety of NADP. The calculated parameters for the two binding modes are reported in Table 3.

The results suggest that ceruchinol could be a modulator of the selected target.

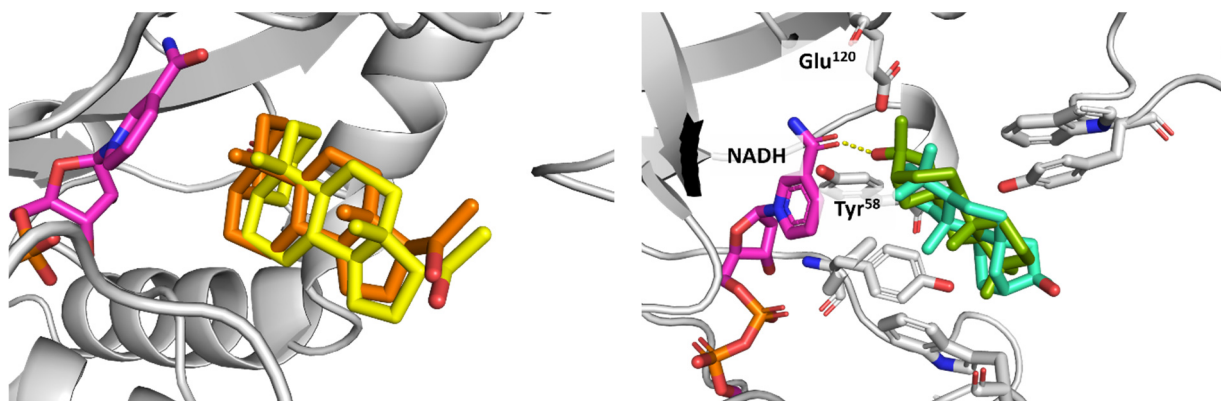


Figure 14. (Left). Result of the control docking simulation. The co-crystallized ligand is shown in orange and the redocked ligand is shown in yellow. (Right) Result of the docking simulation of ceruchinol. Pose 1 is shown in green and pose 2 is shown in cyan.

3.7. 17 β -HSD1 (17 β -Hydroxysteroid Dehydrogenase)

We examined the X-ray crystal structures of Estradiol 17 β -dehydrogenase 1 (17 β -HSD1) deposited in the PDB database and selected 15 human X-ray structures available (resolution = 1.5–3.5 Å). From these (Figure 15), PDB entry 3KLM was chosen to perform the docking since it contains 5 α -dihydrotestosterone (ID: DHT), which partially resembles ceruchinol (see Figure 16).

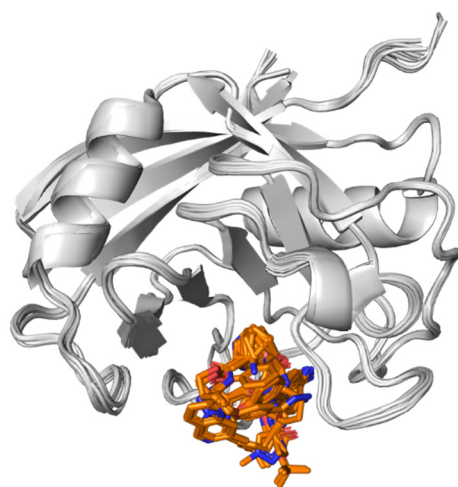


Figure 15. Superposition of the selected 17 β -HSD1 structural models. Co-crystallized ligands are shown in orange. The 15 structures are shown to demonstrate that the binding site is the same for all of them, as well as the alignment of the structures.

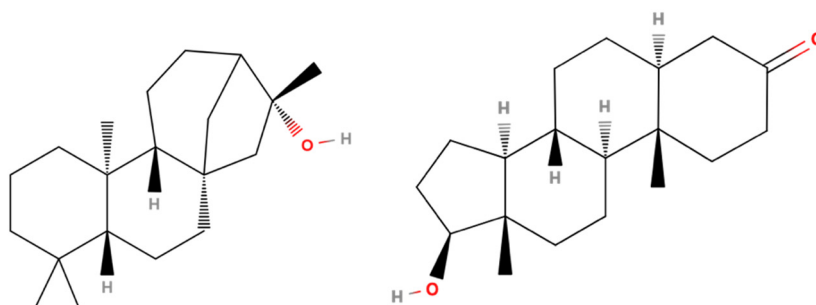


Figure 16. Chemical structure of (left) ceruchinol and (right) 5 α -dihydrotestosterone (ID: DHT).

The result of the docking of DHT and ceruchinol are shown in Figure 17 (top left and right images). Notably, the PDB structure 3KLM shows two alternative binding modes for DHT. This suggests that the natural ligand is not able to establish specific interactions with the target protein, and binding is mainly guided by size and shape complementarity. Therefore, the fact that docking does not reproduce accurately the X-ray binding mode is not surprising. Indeed, the first binding mode is mimicked by pose 4 (Figure 17 down left) and the second arrangement by pose 9 (Figure 17 down right). In both cases, the control ligand does not exactly overlay the X-ray structure, but the poses are acceptable. The energies and docking score calculated for the redocking simulation are reported in Table 4.

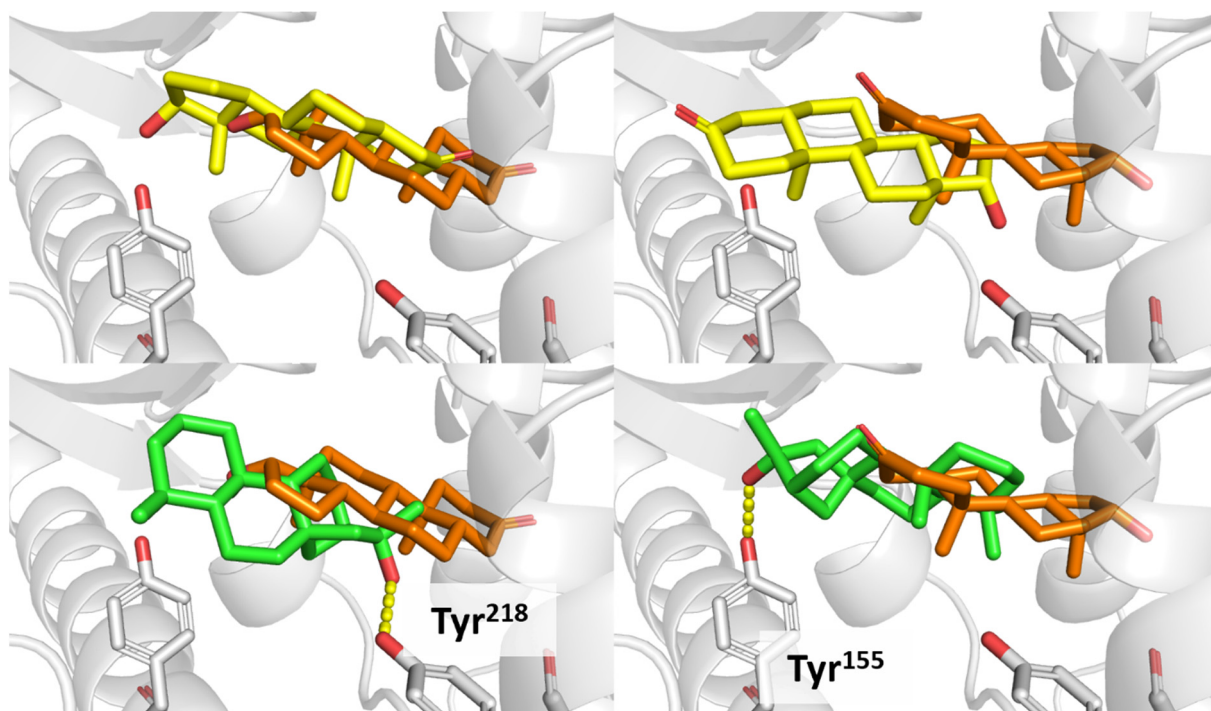


Figure 17. Results of the control docking simulation for (top left) the first and (top right) the second proposed binding mode and docking simulation of ceruchinol in (down left) pose 4 and (down right) pose 9. The co-crystallized ligand is shown in orange, the redocked ligand in yellow, and the docking simulation of ceruchinol is shown in green.

Table 4. Total energy, interaction energy, and docking score for the simulated poses of ligand DHT and ceruchinol.

		Total Energy (kcal/mol)	Interaction Energy (kcal/mol)	Docking Score (kcal/mol)
Ligand DHT	Pose 4	61.8	−23.4	−8.7
	Pose 9	62.7	−22.2	−8.1
Ceruchinol	Pose 1	31.3	−24.3	−8.4
	Pose 3	33.3	−23.4	−8.8

Docking of ceruchinol generated two putative poses, each of which is partially superimposed to the two X-ray orientations of DHT (see Figure 17 and Table 4). The binding mode of ceruchinol features the same pattern of non-polar interactions as DHT, but also tends to form an additional H-bond with a vicinal Tyr residue (Tyr²¹⁸ in pose 1 and Tyr¹⁵⁵ in pose 2). Nevertheless, the formation of this interaction should be taken with caution on

the basis of the X-ray data. Keeping this in mind, we can assume that ceruchinol is a good candidate to be used as an inhibitor modulator for 17 β -HSD1.

4. Discussion

Our investigation into the *P. patens* profile sheds light on its chemical composition and structural intricacies, highlighting its significance in the terrestrial adaptation of plants. The similarities observed with flowering plants, coupled with the evolutionary conservation of key genes, underscore the importance of the cuticle in regulating water status and providing protection against environmental stressors.

The detection of some gibberellin precursors may suggest their potential role as plant hormones in the maturation processes of *P. patens* [45]. Additionally, the presence of C16 and C18 fatty acids may imply their involvement as promoters for the cutin layer, among other functions. The identification of indole-3-acetic acid (IAA), a type of auxin, further emphasizes the nuanced interplay of hormonal and structural factors contributing to the development of wax layers in *P. patens* gametophores [22,23,25,26,42].

The extraction with supercritical CO₂ provided information on the less water-soluble components, and ceruchinol reappeared as the predominant compound, together with other kaurane derivatives. The detection of possible substrates or products of suberin polymerization reinforces our assumptions about the complex molecular composition of the protonemata and gametophores of *P. patens*, besides further enhancing water conservation and adaptation to diverse environmental conditions. The presence of ceruchinol in *P. patens* has been described [33,46], but no such complete determination of the *P. patens* molecular profile has been possible to date, as this compound, in the field, is difficult to find due to its minimal concentration and present only for a few months of the year. In any case, the low concentration of Kaurene could be argued as well due to its high volatility [47].

The identified compounds, especially ceruchinol, open new ways for further research into their potential commercial applications and offer a bioinspired perspective for future studies. The comprehensive insights gained from this investigation enhance our knowledge of the ecological and biotechnological culture success of *P. patens*. It provides a foundation as well for continued exploration in the field of plant adaptation to terrestrial environments and the possibility of a biotechnological cultivation in the laboratory.

To further elucidate potential topical application effects of these extracts on human skin, an in-silico approach was used to study possible interactions between ceruchinol and candidates from several databases of possible targets and interactions [44,48].

In our in-silico experiments targeted Estradiol 17 β -dehydrogenase 1 (17 β -HSD1), it appears that ceruchinol, mostly present as a major component of the CO₂ extract, has the potential to inhibit the catalyzed conversion of estrogen E1 to the more active E2 (Figure 18). This inhibitory effect is noteworthy, as it suggests a mechanism for controlling local E2 levels by targeting 17 β -HSD1 [49,50]. However, our coupling study could not deliver a proper effect on that interaction. Furthermore, ceruchinol is under research for its ability to modulate the activity of AKR1D1. Our coupling study could not deliver a proper effect on that interaction but suggests that ceruchinol would act as a substrate in the catalyzed reaction.

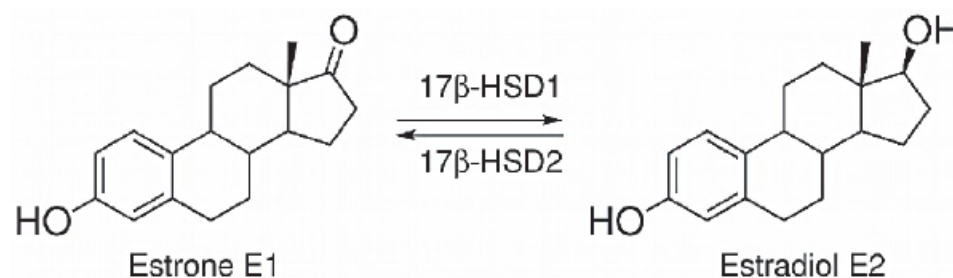


Figure 18. Enzymatic reaction catalyzed by 17- β -dehydrogenase 1 (17 β -HSD1).

Aldo-keto reductase 1D1 (AKR1D1) is a specific member of the AKR family. It is primarily known for its involvement in bile acid synthesis and catalyzes the conversion of 7- α -hydroxycholesterol to 7- α -hydroxy-4-cholesten-3-one, a crucial step in the biosynthesis of cholic acid and chenodeoxycholic acid, which are primary bile acids [51]. Apart from its principal role, AKR1D1 has also been implicated in the metabolism of certain steroid hormones. It can catalyze the conversion of the active steroid hormone cortisol to the inactive form cortisone, contributing as well to the regulation of cortisol levels in the body.

Any alterations or deficiencies in AKR1D1 function can, therefore, impact the balance of cortisol and other steroids in the body, potentially leading to medical conditions related to steroid metabolism. Understanding the enzymatic activity of AKR1D1 is important in the context of endocrinology and the regulation of steroid hormones like cortisol.

Ceruchinol's influence on the enzyme AKR1D1 introduces an intriguing dimension in the realm of cortisol metabolism. If ceruchinol does, indeed, exert an impact on AKR1D1 activity, it could seem significant in the regulation of cortisol levels within the physiological status quo.

Due to the in-silico results, where they could postulate only a modulation from its activity but not a specific one, this team would, nevertheless, propose some hypothetical scenarios:

Ceruchinol as an AKR1D1 inhibitor: In the supposition that ceruchinol acts as an inhibitor of AKR1D1, it may theoretically impair the conversion of cortisone to cortisol. This theoretical modulation might result in diminished cortisol levels in the physiological framework, potentially holding implications for pathologies characterized by hypercortisolism, exemplified by Cushing's syndrome (thin and fragile skin, stretch marks, acne, and skin infections, hirsutism, and hyperpigmentation). This would mechanistically and theoretically be in line with the potential inactivation of the 17 β -dehydrogenase 1 enzyme [52–54].

Ceruchinol as an AKR1D1 activator: In contrast, should ceruchinol amplify the enzymatic activity of AKR1D1, it could facilitate the conversion of cortisone to cortisol, possibly culminating in elevated cortisol concentrations [55,56]. This could be beneficial in circumstances necessitating cortisol replacement therapy, but, nevertheless, as we had the opposite direction with the previous target, 17 β -HSD1, this supposition seems to be less plausible as a matter of submitting a broader view of ceruchinol regulation.

The docking analysis proposed a possible third way of interaction with ceruchinol. The CAR, a member of the nuclear receptor superfamily, underscores a multifaceted and context-dependent relationship [45,57,58]. One discernible facet of this interaction is estradiol's capacity to modulate the transcriptional activity of drug-metabolizing enzymes and transporters, many of which fall under the purview of CAR-mediated regulation. This phenomenon may act as estradiol-induced alterations in the expression of cytochrome P450 enzymes [59–61].

Crucially, the regulation of this crosstalk among distinct receptors in response to hormonal cues has been the subject of extensive investigation and should be further extended. While CAR typically responds to xenobiotics and select pharmaceutical agents, it is not so naïf to extend the influence of endogenous entities such as estradiol [62].

To conclude, it is worth remarking that the actual ramifications of ceruchinol regulation and possible effects along AKR1D1, androstan receptors, 17 β -HSD1, and cortisol metabolism necessitate comprehensive elucidation through exhaustive laboratory and further clinical investigations beyond cosmetic science. The therapeutic or medical utility of such insights hinges on the precise nature of ceruchinol's interaction with the enzyme and the specific context of the clinical condition under consideration.

Subsequent research endeavors are imperative to ascertain whether ceruchinol may be harnessed to modulate cortisol levels and mitigate pathologies linked to cortisol dysregulation [63].

Supplementary Materials: The following supporting information can be downloaded at: <https://www.mdpi.com/article/10.3390/app14031274/s1>. Figure S1: GC-MS profile from the supercritical CO₂ extract without zoom. Total ion current obtained. Ceruchinol was detected at Tr = 71.21 min

(red arrow) and corresponds to the majority peak. Figure S2. Alignments of the sequences of CAR proteins from human (query; Uniprot Q14994) and *M. musculus* (Sbjct; Uniprot O35627) species.

Author Contributions: Conceptualization, S.P.; Methodology, C.M., K.S., B.H., S.P., R.R. and F.W.; Validation, S.P. and C.M.; Formal analysis, C.M., J.H. and S.L.; Investigation, C.M., S.P. and F.W.; Data curation, J.H.; Writing—original draft, C.M., K.S., B.H., J.H., S.L., S.P., R.R. and F.W.; Supervision, S.P.; Project administration, B.H. and S.P. All authors have read and agreed to the published version of the manuscript.

Funding: This research was funded by Mibelle Group Biochemistry, Mibelle AG.

Institutional Review Board Statement: The study did not require ethical approval.

Informed Consent Statement: Not applicable.

Data Availability Statement: The data presented in this study are available on request from the corresponding author. The data are not publicly available due to commercial reasons.

Acknowledgments: We thank Pharmacelera and in special to Javier Luque and Fernando Martín for their collaboration and contribution to the identification of novel potential targets through the use of its proprietary technology, PharmScreen® [39]. We thank NatExplore and ISIPCA for the collaboration.

Conflicts of Interest: The authors declare no conflict of interest.

References

1. Kozgunova, E.; Yoshida, M.W.; Reski, R.; Goshima, G. Spindle motility skews division site determination during asymmetric cell division in *Physcomitrella*. *Nat. Commun.* **2022**, *13*, 2488. [[CrossRef](#)] [[PubMed](#)]
2. Chater, C.C.; Caine, R.S.; Tomek, M.; Wallace, S.; Kamisugi, Y.; Cuming, A.C.; Lang, D.; MacAlister, C.A.; Casson, S.; Bergmann, D.C.; et al. Origin and function of stomata in the moss *Physcomitrella patens*. *Nat. Plants* **2016**, *2*, 16179. [[CrossRef](#)] [[PubMed](#)]
3. Horst, N.A.; Katz, A.; Pereman, I.; Decker, E.L.; Ohad, N.; Reski, R. A single homeobox gene triggers phase transition, embryogenesis and asexual reproduction. *Nat. Plants* **2016**, *2*, 15209. [[CrossRef](#)]
4. Lueth, V.M.; Reski, R. Mosses. *Curr. Biol.* **2023**, *33*, R1163–R1185. [[CrossRef](#)]
5. Lang, D.; van Gessel, N.; Ullrich, K.K.; Reski, R. The genome of the model moss *Physcomitrella patens*. *Adv. Bot. Res.* **2016**, *78*, 97–140.
6. Reski, R. Quantitative moss cell biology. *Curr. Opin. Plant Biol.* **2018**, *46*, 39–47. [[CrossRef](#)]
7. Reski, R.; Bae, H.; Simonsen, H.T. *Physcomitrella patens*, a versatile synthetic biology chassis. *Plant Cell Rep.* **2018**, *37*, 1409–1417. [[CrossRef](#)]
8. Decker, E.L.; Alder, A.; Hunn, S.; Ferguson, J.; Lehtonen, M.T.; Scheler, B.; Kerres, K.L.; Wiedemann, G.; Safavi-Rizi, V.; Nor-dzieke, S.; et al. Strigolactone biosynthesis is evolutionarily conserved, regulated by phosphate starvation and contributes to resistance against phytopathogenic fungi in a moss, *Physcomitrella patens*. *New Phytol.* **2017**, *216*, 455–468. [[CrossRef](#)]
9. Koselski, M.; Hoernstein, S.N.W.; Wasko, P.; Reski, R.; Trebacz, K. Long-distance electrical and calcium signals evoked by hydrogen peroxide in *Physcomitrella*. *Plant Cell Physiol.* **2023**, *64*, 880–892. [[CrossRef](#)] [[PubMed](#)]
10. Resemann, H.C.; Herrfurth, C.; Feussner, K.; Hornung, E.; Ostendorf, A.K.; Gömann, J.; Mittag, J.; van Gessel, N.; de Vries, J.; Ludwig-Müller, J.; et al. Convergence of sphingolipid desaturation across over 500 million years of plant evolution. *Nat. Plants* **2021**, *7*, 219–232. [[CrossRef](#)]
11. Reski, R. Enabling the water-to-land transition. *Nat. Plants* **2018**, *4*, 67–68. [[CrossRef](#)]
12. Moreira, A.S.; Braz-Filho, R.; Mussi-Dias, V.; Vieira, I.J. Chemistry and Biological Activity of Ramalina Lichenized Fungi. *Molecules* **2015**, *20*, 8952–8987. [[CrossRef](#)] [[PubMed](#)]
13. Jones, R.E. The Lichen Genus Ramalina in the Gulf South Region of the United States. Master's Thesis, Graduate School, Louisiana State University, Baton Rouge, LA, USA, 1973.
14. Horst, N.A.; Reski, R. Alternation of generations—Unravelling the underlying molecular mechanism of a 165-year-old botanical observation. *Plant Biol.* **2016**, *18*, 549–551. [[CrossRef](#)] [[PubMed](#)]
15. Lüth, V.M.; Rempfer, C.; van Gessel, N.; Herzog, O.; Hanser, M.; Braun, M.; Decker, E.L.; Reski, R. A *Physcomitrella* PIN protein acts in spermatogenesis and sporophyte retention. *New Phytol.* **2023**, *237*, 2118–2135. [[CrossRef](#)] [[PubMed](#)]
16. Marttinen, E.M.; Decker, E.L.; Heinonen, P.; Reski, R.; Valkonen, J.P. Putative NAD(P)-binding Rossmann fold protein is involved in chitosan-induced peroxidase activity and lipoxygenase expression in *Physcomitrium patens*. *Mol. Plant-Microbe Interact.* **2023**, *36*, 682–692. [[CrossRef](#)] [[PubMed](#)]
17. Marttinen, E.M.; Lehtonen, M.T.; van Gessel, N.; Reski, R.; Valkonen, J.P.T. Viral suppressor of RNA silencing in vascular plants also interferes with the development of the bryophyte *Physcomitrella patens*. *Plant Cell Environ.* **2021**, *45*, 220–235. [[CrossRef](#)]
18. Glime, J.M. Water Relations: Leaf Strategies—Cuticles and Waxes. In *Bryophyte Ecology. Volume 1. Physiological Ecology*; Glime, J.M., Ed.; Michigan Technological University: Houghton, MI, USA, 2007; Chapter 7-4b.

19. Renault, H.; Alber, A.; Horst, N.A.; Lopes, A.B.; Fich, E.A.; Kriegshauser, L.; Wiedemann, G.; Ullmann, P.; Herrgott, L.; Erhardt, M.; et al. A phenol-enriched cuticle is ancestral to lignin evolution in land plants. *Nat. Commun.* **2017**, *8*, 14713. [[CrossRef](#)] [[PubMed](#)]
20. Knosp, S.; Kriegshauser, L.; Tatsumi, K.; Malherbe, L.; Wiedemann, G.; Bakan, B.; Kohchi, T.; Reski, R.; Renault, H. An ancient role for the CYP73 gene family in *t*-cinnamic acid 4-hydroxylation, phenylpropanoid biosynthesis and embryophyte development. *bioRxiv* **2023**. [[CrossRef](#)]
21. Kriegshauser, L.; Knosp, S.; Grienenberger, E.; Tatsumi, K.; Gütle, D.D.; Sørensen, I.; Herrgott, L.; Zumsteg, J.; Rose, J.K.; Reski, R.; et al. Function of the Hydroxycinnamoyl-CoA:Shikimate hydroxycinnamoyl Transferase is evolutionarily conserved in embryophytes. *Plant Cell* **2021**, *33*, 1472–1491. [[CrossRef](#)]
22. Resemann, H.C.; Lewandowska, M.; Gömann, J.; Feussner, I. Membrane lipids, waxes and oxylipins in the moss model organism *Physcomitrella patens*. *Plant Cell Physiol.* **2018**, *60*, 1166–1175. [[CrossRef](#)]
23. Buda, G.J.; Barnes, W.J.; Fich, E.A.; Park, S.; Yeats, T.H.; Zhao, L.; Domozych, D.S.; Rose, J.K. An ATP binding cassette transporter is required for cuticular wax deposition and desiccation tolerance in the moss *Physcomitrella patens*. *Plant Cell* **2013**, *25*, 4000–4013. [[CrossRef](#)] [[PubMed](#)]
24. Jang, G.; Dolan, L. Auxin promotes the transition from chloronema to caulonema in moss protonema by positively regulating PpRSL1 and PpRSL2 in *Physcomitrella patens*. *New Phytol.* **2011**, *192*, 319–327. [[CrossRef](#)] [[PubMed](#)]
25. Miyazaki, S.; Nakajima, M.; Kawaide, H. Assays of protonemal growth responses in *Physcomitrella patens* under blue- and red-light stimuli. *Methods Mol. Biol.* **2019**, *1924*, 35–43. [[PubMed](#)]
26. Lee, S.B.; Yang, S.U.; Pandey, G.; Kim, M.S.; Hyoung, S.; Choi, D.; Shin, J.S.; Suh, M.C. Occurrence of land-plant-specific glycerol-3-phosphate acyltransferases is essential for cuticle formation and gametophore development in *Physcomitrella patens*. *New Phytol.* **2020**, *225*, 2468–2483. [[CrossRef](#)] [[PubMed](#)]
27. Bendz, G.; Santesson, J.; Wachtmeister, C.A.; Kristiansen, L.A.; Jensen, K.A. Study on the chemistry of lichens, the chemistry of the Ramalina ceruchis group. *Acta Chem. Scand.* **1965**, *19*, 1185–1187. [[CrossRef](#)]
28. Erxleben, A.; Gessler, A.; Vervliet-Scheebaum, M.; Reski, R. Metabolite profiling of the moss *Physcomitrella patens* reveals evolutionary conservation of osmoprotective substances. *Plant Cell Rep.* **2012**, *31*, 427–436. [[CrossRef](#)]
29. Huneck, S.; Vevle, O. Inhaltsstoffe der Moose VIII. (-)-16- α -Hydroxykauran aus *Anthelia julacea* (L.) Dum. und *Anthelia juratzkana* (Limpr.) Trev. *Z. Naturforsch.* **1970**, *25*, 227. [[CrossRef](#)]
30. Nilsson, E. (-)-16- α -Hydroxykaurane from *Saellania glaucescens* (Hedw.) Broth. *Acta Chem. Scand.* **1971**, *25*, 4. [[CrossRef](#)]
31. Lehn, J.-M.; Huneck, S.Z. Die erstmalige Isolierung des Diterpens (-)-16- α -Hydroxykauran aus einer Flechte. *Z. Naturforsch.* **1965**, *20*, 1013. [[CrossRef](#)]
32. Fujita, E.; Johne, S.; Kasai, R.; Node, M.; Tanaka, O.; Fujita, E.; Node, M. Diterpenoids of *Rabdosia* species. *Progr. Chem. Org. Nat. Prod.* **1984**, *46*, 77–157.
33. Hayashi, K.-I.; Kawaide, H.; Notomi, M.; Sakigi, Y.; Matsuo, A.; Nozaki, H. Identification and functional analysis of bifunctional ent-kaurane synthase from the moss *Physcomitrella patens*. *FEBS Lett.* **2006**, *580*, 6175–6181. [[CrossRef](#)] [[PubMed](#)]
34. von Schwartzberg, K.; Schultze, W.; Kassner, H. The moss *Physcomitrella patens* releases a tetracyclic diterpene. *Plant Cell Rep.* **2004**, *22*, 780–786. [[CrossRef](#)] [[PubMed](#)]
35. Kerboua, M.; Ahmed, M.A.; Samba, N.; Aitfella-Lahlou, R.; Silva, L.; Boyero, J.F.; Raposo, C.; Rodilla, J.M.L. Phytochemical investigation of new Algerian lichen species: *Physcia mediterranea* Nimis. *Molecules* **2021**, *26*, 1121. [[CrossRef](#)] [[PubMed](#)]
36. Hohe, A.; Decker, E.; Gorr, G.; Schween, G.; Reski, R. Tight control of growth and cell differentiation in photoautotrophically growing moss (*Physcomitrella patens*) bioreactor cultures. *Plant Cell Rep.* **2002**, *20*, 1135–1140. [[CrossRef](#)]
37. Schween, G.; Gorr, G.; Hohe, A.; Reski, R. Unique tissue-specific cell cycle in *Physcomitrella*. *Plant Biol.* **2003**, *5*, 50–58. [[CrossRef](#)]
38. Reski, R.; Abel, W.O. Induction of budding on chloronemata and caulonemata of the moss, *Physcomitrella patens*, using isopen-tenyladenine. *Planta* **1985**, *165*, 354–358. [[CrossRef](#)]
39. Vázquez, J.; Deplano, A.; Herrero, A.; Ginex, T.; Gibert, E.; Rabal, O.; Oyarzabal, J.; Herrero, E.; Luque, F.J. Development and validation of molecular overlays derived from three-dimensional hydrophobic similarity with PharmScreen. *J. Chem. Inf. Model.* **2018**, *58*, 1596–1609. [[CrossRef](#)]
40. Santos, K.B.; Guedes, I.A.; Karl, A.L.; Dardenne, L.E. Highly flexible ligand docking: Benchmarking of the DockThor program on the LEADS-PEP protein-peptide dataset. *J. Chem. Inf. Model.* **2020**, *60*, 667–683. [[CrossRef](#)]
41. Helliwell, C.A.; Poole, A.; Peacock, W.J.; Dennis, E.S. Arabidopsis ent-Kaurene Oxidase catalyzes three steps of gibberellin biosynthesis. *Plant Physiol.* **1999**, *119*, 507–510. [[CrossRef](#)]
42. Ricci, E.J. Investigating the Leaf Cuticle of the Moss *Physcomitrella patens*. Master's Thesis, Rhode Island College: Providence, RI, USA, 2013.
43. Guetchueng, S.T.; Nahar, L.; Ritchie, K.J.; Ismail, F.; Wansi, J.D.; Evans, A.R.; Sarker, S.D. Kaurane diterpenes from the fruits of *Zanthoxylum lepreurii*. *Rec. Nat. Prod.* **2017**, *11*, 304–309.
44. Horn, A.; Pascal, A.; Lončarević, I.; Marques, R.V.; Lu, Y.; Miguel, S.; Bourgaud, F.; Thorsteinsdóttir, M.; Cronberg, N.; Becker, J.D.; et al. Natural products from bryophytes: From basic biology to biotechnological applications. *Crit. Rev. Plant Sci.* **2021**, *40*, 191–217. [[CrossRef](#)]
45. Kawamoto, T.; Kakizaki, S.; Yoshinari, K.; Negishi, M. Estrogen activation of the nuclear orphan receptor CAR (constitutive active receptor) in induction of the mouse Cyp2b10 gene. *Mol. Endocrinol.* **2000**, *14*, 1897–1905. [[CrossRef](#)]

46. Chen, F.; Ludwiczuk, A.; Wei, G.; Chen, X.; Crandall-Stotler, B.; Bowman, J.L. Terpenoid secondary metabolites in bryophytes: Chemical diversity, biosynthesis and biological functions. *Crit. Rev. Plant. Sci.* **2018**, *37*, 210–231. [[CrossRef](#)]
47. Otsuka, M.; Kenmoku, H.; Ogawa, M.; Okada, K.; Mitsuhashi, W.; Sassa, T.; Kamiya, Y.; Toyomasu, T.; Yamaguchi, S. Emission of ent-Kaurene, a diterpenoid hydrocarbon precursor for gibberellins, into the headspace from plants. *Plant Cell Physiol.* **2004**, *45*, 1129–1138. [[CrossRef](#)]
48. Lai, J.-J.; Chang, P.; Lai, K.-P.; Chen, L.; Chang, C. The role of androgen and androgen receptor in skin-related disorders. *Arch. Dermatol. Res.* **2012**, *304*, 499–510. [[CrossRef](#)]
49. Grymowicz, M.; Rudnicka, E.; Podfigurna, A.; Napierala, P.; Smolarczyk, R.; Smolarczyk, K.; Meczekalski, B. Hormonal effects on hair follicles. *Int. J. Mol. Sci.* **2020**, *28*, 5342. [[CrossRef](#)]
50. Wandrey, F.; Henes, B.; Züllig, F.; Reski, R. Biotechnologically produced moss active improves skin resilience. *SOFW J.* **2018**, *144*, 34–37.
51. Imfeld, D. Inhibition of cutaneous cortisol activation: A novel approach to protect skin from stress induced damage and aging. In Proceedings of the 30th IFSCC Congress, Munich, Germany, 18–21 September 2018; Poster IFSCC Munich; pp. 1–501.
52. Gambineri, A.; Forlani, G.; Munarini, A.; Tomassoni, F.; Cognigni, G.E.; Ciampaglia, W.; Pagotto, U.; Walker, B.R.; Pasquali, R. Increased clearance of cortisol by 5beta-reductase in a subgroup of women with adrenal hyperandrogenism in polycystic ovary syndrome. *J. Endocrinol. Investig.* **2009**, *32*, 210–218. [[CrossRef](#)]
53. Dahlgren, A.; Kecklund, G.; Theorell, T.; Åkerstedt, T. Day-to-day variation in saliva cortisol—relation with sleep, stress and self-rated health. *Biol. Psychol.* **2009**, *82*, 149–155. [[CrossRef](#)]
54. Dismukes, A.; Shirtcliff, E.; Jones, C.W.; Zeanah, C.; Theall, K.; Drury, S. The development of the cortisol response to dyadic stressors in Black and White infants. *Dev. Psychopathol.* **2018**, *30*, 1995–2008. [[CrossRef](#)] [[PubMed](#)]
55. Nikolaou, N.; Gathercole, L.L.; Marchand, L.; Althari, S.; Dempster, N.J.; Green, C.J.; Van De Bunt, M.; McNeil, C.; Arvaniti, A.; Hughes, B.A.; et al. AKR1D1 is a novel regulator of metabolic phenotype in human hepatocytes and is dysregulated in non-alcoholic fatty liver disease. *Metabolism* **2019**, *99*, 67–80. [[CrossRef](#)] [[PubMed](#)]
56. Nikolaou, N.; Arvaniti, A.; Appanna, N.; Sharp, A.; Hughes, B.A.; Digweed, D.; Whitaker, M.J.; Ross, R.; Arlt, W.; Penning, T.M.; et al. Glucocorticoids regulate AKR1D1 activity in human liver in vitro and in vivo. *J. Endocrinol.* **2020**, *245*, 207–218. [[CrossRef](#)] [[PubMed](#)]
57. Yang, H.; Wang, H. Signaling control of the constitutive androstane receptor (CAR). *Protein Cell* **2014**, *5*, 113–123. [[CrossRef](#)] [[PubMed](#)]
58. Oliviero, F.; Lukowicz, C.; Boussadia, B.; Forner-Piquer, I.; Pascussi, J.M.; Marchi, N.; Mselli-Lakhal, L. Constitutive Androstane Receptor: A peripheral and a neurovascular stress or environmental sensor. *Cells* **2020**, *9*, 2426. [[CrossRef](#)] [[PubMed](#)]
59. Küblbeck, J.; Niskanen, J.; Honkakoski, P. Metabolism-disrupting chemicals and the Constitutive Androstane Receptor CAR. *Cells* **2020**, *9*, 2306. [[CrossRef](#)]
60. Carazo, A.; Dusek, J.; Holas, O.; Skoda, J.; Hyrsova, L.; Smutny, T.; Soukup, T.; Dosedel, M.; Pávek, P. Teriflunomide is an indirect human Constitutive Androstane Receptor (CAR) Activator interacting with Epidermal Growth Factor (EGF) signaling. *Front. Pharmacol.* **2018**, *9*, 993. [[CrossRef](#)]
61. Cherian, M.T.; Chai, S.C.; Chen, T. Small-molecule modulators of the constitutive androstane receptor. *Expert Opin. Drug Metab. Toxicol.* **2015**, *11*, 1099–1114. [[CrossRef](#)]
62. Min, G.; Kim, H.; Bae, Y.; Petz, L.; Kemper, J.K. Inhibitory crosstalk between Estrogen Receptor (ER) and Constitutively Activated Androstane Receptor (CAR): CAR inhibits ER-mediated signaling pathway by squelching p160 coactivators. *J. Biol. Chem.* **2002**, *277*, 34626–34633. [[CrossRef](#)] [[PubMed](#)]
63. Chen, W.; Thiboutot, D.; Zouboulis, C.C. Cutaneous androgen metabolism: Basic research and clinical perspectives. *J. Investig. Dermatol.* **2002**, *119*, 992–1007. [[CrossRef](#)] [[PubMed](#)]

Disclaimer/Publisher’s Note: The statements, opinions and data contained in all publications are solely those of the individual author(s) and contributor(s) and not of MDPI and/or the editor(s). MDPI and/or the editor(s) disclaim responsibility for any injury to people or property resulting from any ideas, methods, instructions or products referred to in the content.